Research Square

Preprints are preliminary reports that have not undergone peer review.
They should not be considered conclusive, used to inform clinical practice,
or referenced by the media as validated information.

A multi-component herbal formulation limits PRRSV replication and reduces PD-L1-high neutrophil abundance in porcine lungs

Jintao Peng
Huazhong Agricultural University
Xu Wang
Huazhong Agricultural University
Wei Zhou
Huazhong Agricultural University
Xin Fan
Huazhong Agricultural University
Dishi Chen
Huazhong Agricultural University
Shijie Li
Huazhong Agricultural University
Pinpin Chen
Huazhong Agricultural University
Hongxia Ding
Huazhong Agricultural University
Deshi Shi
Huazhong Agricultural University
Zutao Zhou
Huazhong Agricultural University
Fangping Zhang
Fujian Aonong Biological Technology Group Incorporation Limited
Yuncai Xiao
xyc88@mail.hzau.edu.cn

Huazhong Agricultural University

Research Article

Keywords: porcine reproductive and respiratory syndrome virus, multi-component herbal formulation, neutrophils, programmed death-ligand 1, lung immune microenvironment, immunomodulation

Posted Date: November 23rd, 2026

DOI: https://doi.org/10.21203/rs.3.rs-11703298/v1

License: This work is licensed under a Creative Commons Attribution 4.0 International License.
Read Full License

Additional Declarations: No competing interests reported.

Abstract

Available PRRSV vaccines protect poorly against heterologous strains, and control still relies on management rather than immunization. We tested APRR (Anti-PRRSV Prescription of Radix et Rhizoma), a chemically defined herbal formulation, in Marc-145 cells and in a pig challenge model. In Marc-145 cells, APRR extract lowered PRRSV titers, viral RNA and nucleocapsid protein in a dose-dependent manner. In pigs, dietary APRR (4 kg/t) lowered clinical scores and rectal temperature, and reduced viral RNA load in lung and spleen. Single-cell profiling of 24,896 lung cells showed that infection expanded neutrophils from 24.9% to 44.8% of all cells and contracted lymphoid compartments. APRR reduced the abundance of a programmed death-ligand 1 (PD-L1)-enriched neutrophil state, returning neutrophil frequency to 21.6%, and weakened predicted neutrophil-to-CD4 + T cell communication via PD-L1/PD-1. APRR also raised IL1R2, an IL-1 decoy receptor, and partially restored effector and memory-associated transcripts (CD3E, GNLY, IL7R, CD44); the exhausted state persisted. PRRSV-infected lungs therefore carry a PD-L1-high, neutrophil-dominated inflammatory state that APRR partially attenuates.

Introduction

Porcine reproductive and respiratory syndrome (PRRS), caused by PRRS virus (PRRSV), is among the costliest diseases of swine production (Cai et al. 2023; Duan et al. 2025; He et al. 2025; Zhang et al. 2022). The virus continues to diversify, which complicates surveillance and vaccine matching (Fiers et al. 2024). Outcome varies with strain, host status and infection stage; the disease typically presents as reproductive failure in sows and respiratory disease in piglets and growing pigs (Fiers et al. 2024).

Two features make PRRSV hard to control. The virus enters macrophage-lineage cells efficiently (Fiers et al. 2024; Liu et al. 2025; Rowland and Brandariz-Nuñez 2024; Zhang and Guo 2022), and infection perturbs innate and adaptive immunity, with delayed virus-specific cellular responses, dysregulated interferon signaling and prolonged immune imbalance (Cai et al. 2023; Fiers et al. 2024). Current live, inactivated and subunit vaccines give only partial protection against heterologous strains, so adjunct antiviral or immunomodulatory strategies are still needed (Fiers et al. 2024; Li et al. 2024).

Multi-component herbal preparations are attractive as antivirals because they can act simultaneously on viral replication and on host responses (Bello-Onaghise et al. 2020; Huang et al. 2021); plant-derived compounds have also been tested against influenza and SARS-CoV-2 (Ribeiro et al. 2025). In the PRRSV field, glycyrrhizin, chlorogenic acid, cryptotanshinone and related molecules have shown antiviral or anti-inflammatory activity (Bello-Onaghise et al. 2020; Cheng et al. 2013; Duan et al. 2015; Huang et al. 2020). How a chemically characterized formulation of this kind alters the immune response to PRRSV in vivo has not been established.

Neutrophils are heterogeneous and long-lived enough to shape tissue injury and adaptive immunity (Burn et al. 2021; Johansson and Kirsebom 2021; Palomino-Segura et al. 2023; Zhang et al. 2024). In the lung, excessive activation and extracellular trap formation aggravate damage, while other neutrophil states acquire suppressive features resembling granulocytic myeloid-derived suppressor cells (Bert et al. 2023;

Castanheira and Kubes 2019; Pan and Lee 2024; Salzmann et al. 2024; Xuan et al. 2024). Neutrophil-associated programmed death-ligand 1 (PD-L1) signaling impairs T-cell responses in several diseases, raising the possibility that a comparable checkpoint operates during PRRSV infection (Kim et al. 2025; Madzime et al. 2021; Ruedas-Torres et al. 2023; Sun et al. 2018; Yamaguchi et al. 2022).

Resolving which cell states carry this checkpoint program requires single-cell resolution. We therefore used scRNA-seq, with regulon inference and cell-cell communication analysis, to map the lung response (Hao et al. 2021; Hao et al. 2024; Heumos et al. 2023; Jovic et al. 2022; Sikkema et al. 2023); comparable designs have resolved immune dynamics in other viral infections (Hu et al. 2025; Kazer et al. 2020; Li et al. 2026; Lim et al. 2025).

We examined APRR (Anti-PRRSV Prescription of Radix et Rhizoma), a chemically characterized multi-component formulation, in Marc-145 cells and in a pig challenge model. Cells received a decoction extract; pigs received APRR in feed at 4 kg/t. APRR suppressed viral replication, reduced disease severity, and altered neutrophil states, T-cell composition and intercellular signaling in infected lungs. The neutrophil PD-L1 program emerged as the central feature of the response, accompanied by an interferon-primed transcriptional signature that shifted in parallel after APRR treatment.

Materials and Methods

APRR powder, in vitro extract preparation, and chemical characterization

APRR is a self-formulated multi-component herbal prescription; its components were ground into powder (preparation in Fig. 1A), and this powder was used as the feed supplement in all in vivo experiments, including the pigs whose serum was used for the in-blood analysis (Table 1, Fig. S10). For in vitro work, a decoction extract was prepared from the powder: 50 g of powder was decocted in 500 mL ultrapure water for 30 min and filtered, and the residue was re-extracted with a further 500 mL for 30 min. The combined filtrates were centrifuged at 10,000 × g for 10 min and the supernatant was concentrated to 50 mL, giving a stock extract of 1 g/mL crude-drug equivalent. The extract was sterilized through a 0.22 μm membrane, and working solutions were prepared fresh before each experiment. The chemical profile was analyzed by high-performance liquid chromatography-mass spectrometry (HPLC-MS; Agilent 1290/6545 Q-TOF, Agilent Technologies, Santa Clara, CA, USA) in positive and negative electrospray ionization modes; compounds were annotated by accurate mass and MS/MS matching against METLIN (https://metlin-nl.scripps.edu/landing_page.php?pgcontent=mainPage), HMDB (https://hmdb.ca) and an in-house traditional Chinese medicine database. In-blood constituents were defined by matching the formula annotation table to serum LC-MS annotations of APRR-treated and control pigs by normalized compound name and HMDB ID; 111 of the 1,198 annotated constituents met this criterion, and their response classification is reported in Results. The 15 most abundant of these 111 constituents (mean signal in APRR-treated pigs from three technical HPLC-MS injections of a single pooled preparation) are listed in Table 1 (Fig. S10).

Table 1

Most abundant in-blood constituents of APRR. Only three of the 15 listed constituents (2,3-dihydroxybenzoic acid, malic acid and citric acid) fall within the 23 significantly altered constituents; abundance ranking therefore reflects exposure rather than response. The 15 most abundant of the 111 constituents detected in the serum of APRR-treated pigs (23 significantly altered versus controls, FDR < 0.05; the remaining 88 not distinguishable from endogenous serum metabolites; Fig. S10) are ranked by mean HPLC-MS signal in APRR (three technical injections of a single pooled APRR preparation); percentages denote each constituent's share of the total signal of the 111 in-blood constituents. Several abundant in-blood constituents (e.g., pyrogallol, choline, betaine, citric acid, malic acid, pyroglutamic acid) are also common endogenous serum metabolites and may partly derive from host metabolism rather than from the formula. After exclusion of these putatively endogenous metabolites, the residual top-15 signal is dominated by oleamide, baicalin, and 12-methyltridecanoic acid, which together account for 64.5% of the total in-blood signal; oleamide and 12-methyltridecanoic acid are themselves putatively endogenous long-chain lipids, so baicalin is the most abundant constituent that can be attributed to the formula with reasonable confidence.

Rank	Constituent	Chemical class	Mean signal (APRR, n = 3)	Share of in-blood signal (%)
1	Oleamide	Fatty amides	1.33×10^{10}	25.3
2	Baicalin	Flavonoids	1.28×10^{10}	24.5
3	Pyrogallol	Shikimates and phenylpropanoids	4.02×10^{9}	7.7
4	12-Methyltridecanoic acid	Fatty acids and conjugates	2.36×10^{9}	4.5
5	Adenine	Nucleobases	1.95×10^{9}	3.7
6	Choline	Quaternary ammonium compounds	1.65×10^{9}	3.1
7	Erucamide	Fatty amides	1.61×10^{9}	3.1
8	Guanine	Nucleobases	9.66×10^{8}	1.8
9	2,3-Dihydroxybenzoic acid	Phenolic acids (C6-C1)	8.78×10^{8}	1.7
10	Betaine	Quaternary ammonium compounds	8.77×10^{8}	1.7
11	Fagomine	Aminosugars and aminoglycosides	8.45×10^{8}	1.6
12	Malic acid	Hydroxy dicarboxylic acids	7.43×10^{8}	1.4
13	Citric acid	Tricarboxylic acids	7.37×10^{8}	1.4
14	Caffeic acid	Phenylpropanoids (C6-C3)	6.90×10^{8}	1.3
15	Pyroglutamic acid	Amino acids and derivatives	6.78×10^{8}	1.3

Statements and Declarations

Cells, virus, and in vitro antiviral assays

Marc-145 cells were maintained in Dulbecco's modified Eagle medium (DMEM; Gibco, Thermo Fisher Scientific, cat. no. C11995500BT, Waltham, MA, USA) supplemented with 10% fetal bovine serum (FBS; SERANA, cat. no. FBS-AUS050, Pessin, Germany). The PRRSV WUH3 strain (PRRSV-2, sublineage 8.7; HP-PRRSV, JXA1/CH-1a-like) was isolated in our laboratory and propagated in Marc-145 cells. For virus stock preparation, inoculated monolayers were allowed to adsorb for 1 h at 37°C and were then maintained in DMEM containing 2% FBS for 3–5 d. When the cytopathic effect exceeded 80%, cells and culture supernatants were subjected to three freeze–thaw cycles and centrifuged at 3,000 × g for 10 min at 4°C, and the clarified supernatant was stored at − 80°C. Viral titers were determined in Marc-145 cells by 10-fold serial dilution with eight replicate wells per dilution and calculated as 50% tissue culture infectious dose ($TCID_{50}$) values by the Reed–Muench method (Reed and Muench 1938) after 5–7 d of observation. Cell viability was measured with a Cell Counting Kit-8 (CCK-8; SERANA, cat. no. CCK500S, Pessin, Germany) assay. Viral replication in APRR-treated cells was evaluated by immunofluorescence staining, absolute quantitative reverse transcription PCR (qRT-PCR) with SPARKscript II All-in-one RT SuperMix (SparkJade, cat. no. AG0305-B, Jinan, China) and 2×SYBR Green qPCR Mix with ROX (SparkJade, cat. no. AH0104-B, Jinan, China) targeting PRRSV open reading frame 7 (*ORF7*), $TCID_{50}$ assay, and Western blot analysis. For Western blot, proteins were extracted with a protease inhibitor cocktail (SparkJade, cat. no. SJ-MX0001-A, Jinan, China), resolved by SDS-PAGE using 5× loading buffer (SparkJade, cat. no. EC0013, Jinan, China), and detected with SuperECL detection reagent (SparkJade, cat. no. EC0086, Jinan, China). A prestained protein marker (10–180 kDa; SparkJade, cat. no. EC2019-B, Jinan, China) was used for size reference, and antibodies were stripped with Western blot stripping buffer (SparkJade, cat. no. ED0022-B, Jinan, China) for reprobing. Antifade mounting medium (SparkJade, cat. no. EE014, Jinan, China) was used for immunofluorescence slide preparation. Western blot quantification was based on three independent experiments (n = 3 membranes, one well per condition per membrane).

Animal experiments

All animal procedures were approved by the Institutional Animal Care and Use Committee of Huazhong Agricultural University (approval no. HZAUSW-2025-0110) and were conducted in accordance with institutional guidelines and the ARRIVE (Animal Research: Reporting of In Vivo Experiments) guidelines. Eighteen weaned piglets (21 days old; Landrace × Large White crossbred), negative for both PRRSV antigen and antibody, were randomly assigned to three groups (n = 6 per group): Control, PRRSV and APRR. The Control and PRRSV groups received the basal diet throughout the study, whereas the APRR group received feed supplemented with APRR at 4 kg/t. After a 3-d acclimation period, the first experimental day was designated day 1. On day 14, pigs in the PRRSV and APRR groups were challenged by intramuscular injection with 2×10^5 TCID50 PRRSV per pig (Chang et al. 2024a), and Control animals received an equal volume of sterile phosphate-buffered saline (PBS). Body weights were recorded on days 1, 14 and 24. Rectal temperature, clinical signs and clinical scores were recorded daily and are

reported as means of all daily observations; two PRRSV pigs and one APRR pig died before the planned day-10 sampling. Blood samples were collected at 3, 6 and 10 d post-infection for serum separation, and pigs were euthanized at 10 d post-infection for collection of serum, lung and spleen samples for viral-load analysis and histopathology. Viral RNA in lung, spleen and serum was quantified with the same absolute qRT-PCR assay against ORF7 described above; tissue values are expressed as log10 genome copies per gram of tissue (three animals per group) and serum values as log10 copies per milliliter of serum (four animals per group).

Single-cell RNA sequencing and bioinformatics analysis

Lung tissues were collected within 10 min after euthanasia, and approximately 1 g of fresh lung tissue encompassing lesion and marginal areas was transferred into precooled MACS Tissue Storage Solution (Miltenyi Biotec, cat. no. 130-100-008, Bergisch Gladbach, Germany). Tissues were minced into pieces of approximately 1 mm^3, digested in DMEM containing 0.2% collagenase IV (Sigma-Aldrich, cat. no. C5138, St. Louis, MO, USA) and 0.01% DNase I (Sigma-Aldrich, cat. no. DN25, St. Louis, MO, USA) at 37°C for 40 min with intermittent agitation, filtered through a 40 μm cell strainer, and subjected to red-blood-cell lysis. The final cell pellet was resuspended in PBS containing 0.04% bovine serum albumin (BSA) and re-filtered through a 40 μm mesh. Cell concentration and viability were determined using an automated cell counter, and only suspensions with viability > 85% were used for library construction.

Libraries were generated with the 10x Genomics Chromium platform using Chromium Next GEM Single Cell 3' Reagent Kits v3.1 (10x Genomics, PN-1000121, Pleasanton, CA, USA) with a target recovery of 8,000 cells per sample according to the manufacturer's instructions. Library concentration and fragment-size distribution were assessed by Qubit 4.0 Fluorometer (Thermo Fisher Scientific, Waltham, MA, USA) and Agilent 2100 Bioanalyzer (Agilent Technologies, Santa Clara, CA, USA), respectively. Qualified libraries were sequenced on an Illumina NovaSeq 6000 (Illumina, San Diego, CA, USA) in paired-end mode at a depth of at least 50,000 reads per cell. Raw FASTQ files were processed with Cell Ranger (v7.0.1; 10x Genomics) to demultiplex cellular barcodes, align reads to the Sscrofa11.1 reference genome using the STAR aligner, and generate gene-cell count matrices.

Downstream analyses were performed using Seurat v5 (Hao et al. 2024) in R 4.4.2. Cells with nFeature_RNA < 200 or > 7,000, nCount_RNA > 50,000, or percent.mt > 15% were filtered out. After normalization and identification of 3,000 highly variable genes (selection.method = "vst"), data were scaled, and principal component analysis (PCA) was performed on the variable genes. Cell clustering was conducted using FindNeighbors (dims = 1:30) and FindClusters (resolution = 0.6), and cells were visualized with uniform manifold approximation and projection (UMAP). Doublets were identified and removed using DoubletFinder (v2.0.4) (McGinnis et al. 2019). Doublet rates by group and sample are shown in Fig. S1F, G. Clusters were manually annotated based on canonical lineage marker gene expression.

Differential expression analysis between groups was performed using FindAllMarkers (min.pct = 0.25, logFC.threshold = 0.25, test.use = 'wilcox'), and Kyoto Encyclopedia of Genes and Genomes (KEGG) pathway enrichment analysis was conducted on differentially expressed genes (Wu et al. 2021). Gene regulatory networks were inferred using SCENIC (Aibar et al. 2017; Bravo González-Blas et al. 2023) via pySCENIC (v0.11.2) with GRNboost2 for coexpression module detection, RcisTarget (hg38 refseq-r80 10 kb up- and downstream-TSS human databases, used as a cross-species proxy because no porcine library is available) for motif enrichment, and AUCell for regulon activity scoring. Intercellular communication was analyzed with CellChat (v1.5.0) (Jin et al. 2021) following established single-cell communication workflows (Heumos et al. 2023; Jovic et al. 2022), scoring ligand–receptor interactions between immune populations at the default significance threshold ($p < 0.05$). Libraries were generated from one animal per group (Control, PRRSV and APRR) with cells pooled within group, yielding 24,896 cells (8,488 / 7,794 / 8,614). Because each group derives from a single animal, group-level comparisons are descriptive point estimates only, and all statistical inference is made at the cell level with false-discovery-rate correction (see Statistical analysis).

Ligand activity was ranked with a literature-curated ligand–target scoring scheme, because no porcine ligand–target matrix is available for prior-based inference. For each secreted ligand detected in the sending compartment, a target set was assembled from published IL-1, TNF, TGF-β and IFN-γ response programs, and a priority score was computed as $\log1p(\text{total sender expression}) \times (n_{up} - 0.3\, n_{down} + 0.5\, n_{recovery} + 0.5 \max(R, 0)) \times d$, where n_{up} and n_{down} are the numbers of curated targets among genes up- or down-regulated by PRRSV in T cells ($P < 0.05$, $|\log2\ FC| > 0.25$), $n_{recovery}$ is the number of targets among genes restored toward Control by APRR, R is the net regulation of the cognate receptors in the same comparison, and d is a curated direction weight (+ 1 exhaustion-promoting, + 0.5 mixed, + 0.3 IFN-γ, -1 recovery-promoting). The score ranks curated hypotheses; it is not an unbiased estimate of ligand activity and is not treated as independent mechanistic evidence.

Pathway activity was scored per cell by single-sample gene set enrichment analysis (ssGSEA; GSVA 2.0.7, ssgsea.norm = TRUE) over 12 curated gene sets of 4 to 15 genes each, scored against the full transcriptome (17,336 genes detected in the porcine annotation). The sets were interferon-α response (ISG15, IFIT1, IFIT2, IFIT3, MX1, MX2, OAS1, OAS2, OASL, RSAD2, ISG20, IRF7, IRF9, STAT1, STAT2), interferon-γ response (GZMB, CXCL9, CXCL10, CIITA, NLRC5, IRF1, STAT1, GBP1, GBP5), IL-1/NF-κB signaling (NFKB1, NFKBIA, RELA, IL1B, CXCL8, TNF, CCL2, PTGS2), TNF signaling (TNFAIP3, NFKBIA, CXCL2, CCL20, JUNB, NFKB2), apoptosis (CASP3, CASP8, BAX, BCL2, BIRC3, TNFRSF10B), hypoxia (HIF1A, VEGFA, LDHA, SLC2A1, PGK1), epithelial–mesenchymal transition (CDH2, VIM, SNAI1, TWIST1, FN1, ACTA2), T-cell activation (CD3D, CD8A, GZMK, GZMB, IL2RG, LCK), neutrophil degranulation (MPO, ELANE, CXCL8, S100A8, S100A9, DEFA1, LCN2), alternative macrophage activation (CD163, MRC1, MSR1, FOLR2, CD209), complement (C1QA, C1QB, C1QC, C3, C4B) and interferon-stimulated antiviral effectors (OAS1, IFIH1, DDX58, MAVS, IRF3, IRF7). Per-cell scores were averaged within cell type and group and are displayed in Fig. S9.

Statistical analysis

Data were presented as mean ± standard deviation (SD). Comparisons between two groups were performed with unpaired Student's t-tests, and comparisons among multiple groups were performed by one-way analysis of variance (ANOVA) followed by Tukey's post hoc test. Welch's correction was applied where group variances differed markedly, as for serum IL-1β ($P = 4.5 \times 10^{-4}$) and lung p-p65 ($P = 8.2 \times 10^{-4}$). Statistical significance was determined based on $P < 0.05$. Western blot bands were quantified densitometrically, normalized to β-actin on the same membrane and expressed relative to the virus-only lane of that membrane; the three membranes were treated as independent replicates and compared by paired t-test (n = 3 membranes). For the scRNA-seq differential-expression analyses, between-group comparisons were performed at the cell level with Wilcoxon rank-sum tests and corrected for multiple testing using the Benjamini–Hochberg procedure; because each group is represented by a single animal, these cell-level P values are descriptive and no inference across biological replicates is claimed. For the confirmatory wet-lab endpoints, sample sizes were IL-1β serum ELISA (n = 6 animals per group) and lung p-p65 immunofluorescence (n = 4 animals per group); two-group comparisons used Welch's t-test given unequal variances. Accordingly, the single-cell results are reported as exploratory, hypothesis-generating observations rather than hypothesis-testing evidence, and no causal or population-level inference is drawn from them.

Results

APRR inhibits PRRSV replication in vitro and lowers lung and spleen viral load in pigs

In vitro, APRR was not cytotoxic to Marc-145 cells at concentrations up to 1,000 μg/mL, although cell viability fell at 10,000 μg/mL (Fig. 1B). PRRSV-N immunofluorescence decreased with increasing APRR concentration (Fig. 1C), and both infectious titer in culture supernatant and absolute PRRSV ORF7 copy number declined dose-dependently (Fig. 1D, E); N protein normalized to β-actin followed the same gradient (Fig. 1F, G). In the pig challenge model (design in Fig. 1H; body weight and rectal temperature in Fig. 1I), dietary APRR at 4 kg/t lowered lung viral RNA from 9.20 ± 0.17 to 7.86 ± 0.40 log10 copies per g of tissue ($P = 0.006$) and spleen viral RNA from 8.17 ± 0.47 to 7.35 ± 0.19 log10 copies per g of tissue ($P = 0.048$; unpaired t-test, n = 3 per group). Daily clinical scores fell from 4.83 ± 2.89 to 3.39 ± 2.18 and mean rectal temperature from 40.67 ± 0.66 to 40.16 ± 0.45°C; both are means of all daily observations (66, 63 and 65 scores and 66, 64 and 66 temperature readings for Control, PRRSV and APRR; Fig. 1J, K). Two PRRSV pigs and one APRR pig died before day 10, whereas all control pigs survived. Serum viral RNA at 10 d post-infection was 0.85 log10 lower than in the PRRSV group (7.94 ± 0.87 vs 7.08 ± 0.42 log10 copies per mL of serum; n = 4 per group) without reaching significance, although the direction of the difference was the same at 3, 6 and 10 d post-infection.

Lung tissue from the three groups was profiled by scRNA-seq (workflow, Fig. 2A). After SCTransform normalization and Harmony correction, 24,896 cells were integrated into twelve major cell types (8,488 Control / 7,794 PRRSV / 8,614 APRR) and annotated by canonical markers (Fig. 2B, C). Each group is a

single library, so the proportions and cell-level statistics reported below are descriptive and do not estimate between-animal variation. Neutrophils rose from 24.9% of cells in Control to 44.8% in PRRSV, lymphoid compartments contracted correspondingly, and under APRR neutrophil frequency returned to 21.6%, slightly below the Control value (Fig. 2D, E). Per-group UMAPs, QC metrics and doublet rates were balanced across groups (Fig. S1); entry receptors and macrophage ISG rescue are in Fig. S2, cell-proportion pies in Fig. S8, and lineage-marker module scores in Fig. S11.

Per-group UMAPs recovered the same major cell types in all three groups (Fig. S1A–C). Features and counts per cell were balanced across groups (Fig. S1D, E), and removal of doublets with DoubletFinder left a low, balanced doublet rate across groups and samples (Fig. S1F–H).

CD163, SIGLEC1 and SPP1 were expressed mainly in macrophages and monocytes, with group-specific shifts (Fig. S2A–E). APRR partially restored interferon-stimulated gene expression in macrophages relative to PRRSV, resolved across macrophage subclusters (Fig. S2F–J).

APRR reduces PD-L1-high neutrophil abundance and remodels inflammatory states

The compositional shift is expanded as cell-proportion pies (Fig. S8A–D), and the lineage-marker module scores used for annotation as heat maps (Fig. S11A, B).

Neutrophils, the most expanded population in Fig. 2, resolved into three states defined by state-specific markers: pdl1 (PD-L1^{+}, immunosuppressive; CD274, PDCD1LG2, IDO1), isg (ISG15, IFIT1, MX1, OAS1, RSAD2) and proinf (IL1B, TNF, PTGS2, CCL2, CXCL2, S100A12) (Fig. 3A; extended panels in Fig. S3). The pdl1 state accounted for 5.2% of neutrophils in Control, 59.0% in PRRSV (11.3-fold) and 17.2% under APRR (3.3-fold), whereas the isg state fell from 62.8% to 23.6% during infection and returned to 51.3% under APRR (Fig. 3B).

Within pdl1^{+} neutrophils, however, the PD-L1 program score (CD274 + PDCD1LG2 + IDO1) did not fall: Control 0.30, PRRSV 0.97, APRR 1.00 (Fig. 3C). The decline in bulk neutrophil CD274 (0.19 → 1.01 → 0.55; Fig. 3E) therefore reflects the lower abundance of PD-L1-high neutrophils rather than a weaker checkpoint program within them.

IL1R2, which encodes a decoy receptor that binds IL-1β without initiating signaling (Garlanda et al. 2013; McMahan et al. 1991), was the most strongly induced neutrophil transcript under APRR (log2FC + 1.75, padj = 1×10^{-43}). The induction is transcript-level only and the protein was not measured, so the IL1R2 → IL-1β → NF-κB ordering remains inferred (Discussion); it is nonetheless consistent with the lower serum IL-1β in APRR-treated pigs (Fig. 5J), although that link was not tested directly. At the axis level, the composite PD-L1→PD-1 axis-strength index (pdl1^{+} neutrophil abundance × per-cell CD274 × T-cell PD-1, normalized to Control) rose from 1.0× in Control to 46.8× in PRRSV and fell to 9.3× under APRR, attenuated but not restored to baseline (Fig. 3G).

Neutrophil DEGs are shown as a dual volcano (Fig. 3H). In the PRRSV-versus-Control contrast the most up-regulated transcripts were NF-κB / IL-1 module genes (IL1B, IL1A, TNFAIP2, NFKBIA, NFKBIZ, IRAK3, IKBKB, NFKB2), so infection activated this module transcriptionally. In the APRR-versus-PRRSV contrast IL1R2 was the leading up-regulated transcript (log2FC + 1.75, padj = 1×10^{-43}), while the NF-κB module (NFKBIA, NFKBIZ, NFKB2, TRAF1) and the PD-L1 axis (CD274, PDCD1LG2, IDO1) moved to the down-regulated side and ISG effectors (ISG15, MX1, RSAD2) moved up. KEGG enrichment of the APRR-altered set (Fig. 3I) resolved the same two directions: NF-κB, TNF and NOD-like receptor signaling down, interferon and antiviral modules up.

Extended neutrophil panels support the Fig. 3 annotation: subcluster UMAP and combined view (Fig. S3A–C), relative proportions (Fig. S3D), marker dot and feature plots (Fig. S3E, F) and subcluster dot plot (Fig. S3G, H).

SCENIC was used to nominate regulatory programs, with hg38 cisTarget rankings as a cross-species proxy because no porcine library exists; the regulons reported are therefore candidates rather than porcine-validated circuits. Regulon specificity scoring identified lineage transcription factors, with NFIL3, NFE2 and IRF1 prominent in neutrophils (Fig. S7A, B); IRF1 tracked the ISG signature in PRRSV neutrophils and decoupled under APRR. AUC projections, a per-cell-type module heat map and a TF–target network placed IRF1/STAT1-associated regulons among those attenuated by APRR (Fig. S7B–D). These regulons are leads for functional validation.

APRR partially restores T-cell effector programs without reversing the exhausted state in PRRSV-infected lungs

T cells resolved into five states defined by lineage markers: $CD8^+$ Tc (CD8B, CCL5), $CD4^+$ Th (CD4, TNFRSF4), cycling T (UBE2C, DLGAP5), exhausted T (SOX13, BLK) and innate-like T (KIT, KLRB1) (Fig. 4A, B). PRRSV shifted the T-cell compartment toward $CD8^+$ effector and cycling states and away from $CD4^+$ and exhausted states, and APRR moved the composition back toward the Control pattern (Fig. 4D).

On the PD-1 / PD-L1 axis, CD274 on neutrophils rose with PRRSV (0.19 → 1.01, log1p CPM × 10^4) and was relieved by APRR (0.55), whereas PDCD1 on T cells stayed constitutive throughout (0.24 → 0.21 → 0.28) (Fig. 3E, F; Fig. 4C, F). The checkpoint ligand, not the receptor, is the APRR-sensitive node. The $CD8^+$ effector T-cell fraction was 23% of T cells in Control, 53% in PRRSV and 44% under APRR (n = 777 / 1,129 / 1,185 T cells in Control / PRRSV / APRR) (Fig. 4D).

Cytotoxicity transcripts did not shift uniformly. GNLY rose from 0.42 in PRRSV to 1.08 under APRR, above the Control value of 0.92, and IFNG (0.13 → 0.17) and NKG7 (1.14 → 1.27) rose modestly, whereas GZMB was unchanged (0.69 → 0.70) and GZMK (0.34 → 0.16) and PRF1 (0.55 → 0.46) were lower under APRR (Fig. 4E). Among checkpoint transcripts, PDCD1 (0.21 → 0.28) and CTLA4 (0.58 → 0.54) were unchanged, whereas LAG3 (0.65 → 0.89), TIGIT (0.39 → 0.52) and HAVCR2 (0.70 → 0.79) remained elevated and were numerically higher than under PRRSV; none of the five returned toward the Control

level. Progenitor and activation markers moved up: IL7R (0.83 → 1.42, above the Control value of 1.33), CD44 (0.95 → 1.60) and CD69 (0.51 → 0.84), together with TCF7 (0.29 → 0.38) and CCR7 (0.22 → 0.32), which nevertheless remained below Control (Fig. 4E).

Differential expression showed the same asymmetry: PRRSV suppressed the compartment (912 DEGs, 59 up / 853 down vs Control) and APRR reversed most of it (1,299 DEGs, 1,293 up / 6 down vs PRRSV; $P < 0.05$ and $|\log2\ FC| > 0.25$ in both contrasts), with effector (GNLY, IFNG) and checkpoint (LAG3, TIGIT, PDCD1) genes among the changes (Fig. 4G); KEGG enrichment of the restored set resolved rescued cytotoxicity (NK-cell-mediated cytotoxicity, FcγR-mediated phagocytosis) and T-cell receptor signaling alongside the PD-L1/PD-1 checkpoint pathway (Fig. 4H). The per-cell exhaustion score did not fall under APRR (APRR ≈ PRRSV; Fig. 6K), so effector recovery occurred without reversal of the exhaustion program.

Figure 4 APRR partially restores T-cell effector programs without reversing the exhausted state. T cells resolved into five subclusters (A) annotated by lineage-defining markers (B) and a PD-1-axis schema (C). Compositional shift across groups (D). T-cell functional gene programs (E), grouped as cytotoxicity/effector, checkpoint/inhibitory and progenitor/activation; dot fill encodes mean expression. PD-1/PD-L1 axis: ligand relieved, receptor constitutive (F). Dual volcano of PRRSV- and APRR-responsive T-cell DEGs (G). KEGG enrichment of APRR-restored T-cell DEGs (H)

APRR attenuates inferred neutrophil-to-T-cell PD-L1 signaling upstream of the neutrophil state

The neutrophil and T-cell findings converge on a single checkpoint axis. Antigen-presentation machinery was broadly preserved across all twelve cell types in all three groups (Fig. 5A), with the expected PRRSV-induced dampening in monocytes and macrophages and partial-to-full recovery under APRR, so the checkpoint rewiring cannot be attributed to loss of antigen presentation. CellChat inferred macrophages, monocytes and neutrophils as the principal PD-L1 / PD-L2 senders toward $CD4^+$ T cells (Fig. 5B): CD274 → PDCD1 communication was essentially absent in Control, broadly induced by PRRSV, and under APRR selectively reduced on the neutrophil leg while the macrophage leg was retained. Epithelial and ciliated cells sent minimally in every group.

Literature-curated ligand–target scoring ranked IL1B first among candidate exhaustion drivers (priority 2.83), followed by TGFB1 (1.20, neutral role), TNF (1.13, exhaustion), IL6 (0.48), TGFB2 (0.45, neutral) and IL1A (0.33) (Fig. 5C, D). In the APRR-versus-PRRSV ligand → target program (Fig. 5E), LAG3, CTLA4 and PDCD1 induction in PRRSV was released, and NFKB1, STAT3, IL7R, TCF7 and CD28 were re-engaged. A nine-checkpoint summary dot plot (PDCD1, CD274, PDCD1LG2, CTLA4, LAG3, HAVCR2, TIGIT, IDO1, BTLA) (Fig. 5F) showed broad PRRSV induction with a coordinated APRR reversal that was most complete on neutrophils (CD274, IDO1) and only partial on T cells (CTLA4, LAG3, TIGIT, HAVCR2). Macrophage CD274 was modestly higher under APRR (0.28 → 0.50); the neutrophil compartment

remains the dominant PD-L1 sender (1.01 → 0.55), and its reduction accounts for the net checkpoint release in Fig. 5H.

Figure 5G summarizes the mechanism as a dual-axis, four-pillar working model. PRRSV imposes a triple injury (neutrophil-dominated inflammation with elevated IL-1β, neutrophil and macrophage PD-L1 engagement of T-cell PD-1, and ISG antiviral silencing), and APRR opposes it through (i) lower neutrophil PD-L1, releasing the CD274 → PDCD1 checkpoint; (ii) lower IL-1β protein upstream of NF-κB, anchored by IL1R2 induction (log2FC + 1.75, padj = 1×10^{-43}; transcript-level, see Discussion); (iii) rebuilt ISG antiviral output (MX1, RSAD2, ISG15, IRF7; Fig. 3D), reflected in the recovery of the isg neutrophil state from 23.6% to 51.3%; and (iv) reversal of neutrophil infiltration (44.8% → 21.6% of lung cells) with up-regulation of TGF-β and IL-10. Downstream of checkpoint release, CD3E (+ 39%), GNLY (~ 2.7-fold), TCF7 and IL7R were higher under APRR than under PRRSV, while the terminal-exhaustion marker GZMK was lower; GZMB magnitude was comparable between PRRSV and APRR (Fig. 5H, left) and PRF1 was marginally lower under APRR. Inhibitory-checkpoint transcription on T cells was only partly reset: PDCD1 and CTLA4 unchanged, LAG3, TIGIT and HAVCR2 still elevated. Effector recovery occurred without exhaustion reversal, and the schematic makes this distinction explicit. Network pharmacology converged in-blood APRR constituents onto core host-response modules (Fig. S10).

At single-cell resolution (Fig. 5H; n = 777 / 1,129 / 1,185 T cells, Control / PRRSV / APRR), GZMB was comparable between PRRSV and APRR (ns; means 0.52 vs 0.53), whereas the composite recovery score (per-cell mean of GZMB and CD3E) was higher under APRR (1.33 vs 1.03; Mann–Whitney p = 2.4×10^{-58}, a within-sample cell-level test that does not infer across animals; Cohen's d = 0.62) and above Control (1.05; d = 0.58). The gain therefore comes from CD3E, that is, from T-cell identity and recognition, rather than from GZMB magnitude. APRR restores T-cell identity and the effector transcriptional program without reversing exhaustion.

Two independent wet-lab assays tested the downstream arms of the IL-1β → NF-κB branch (Fig. 5I, J). Lung phospho-p65 immunofluorescence rose from 12.3 ± 1.5 in Control to 67.0 ± 7.0 in PRRSV (5.5-fold) and fell to 37.1 ± 4.2 under APRR (44.6% reduction vs PRRSV, p = 8.2×10^{-4}, Welch's t; n = 4 animals per group) (Fig. 5I). Serum IL-1β paralleled this: 61.9 ± 13.4, 176.8 ± 31.7 and 89.2 ± 15.0 pg/mL (49.6% reduction vs PRRSV, p = 4.5×10^{-4}, Welch's t; n = 6 animals per group) (Fig. 5J). The IL1R2 node itself remained transcript-only, and CellChat outputs and ligand–target scores are inferred predictions rather than biochemical evidence.

Of 1,198 annotated APRR constituents, 111 (9.3%) were detectable in the serum of APRR-treated pigs; 23 differed from control pigs (FDR < 0.05) and the remaining 88 were indistinguishable from endogenous serum background (the full profile is in Fig. S10C). Forty-one of the in-blood constituents mapped onto 10 core PRRSV-response genes, forming 14 mechanism-module nodes concentrated in the neutrophil-inflammatory module (15 constituents, with overlaps), the TNF/inflammatory axis (13) and the PD-L1/T-cell exhaustion module (7) (convergence network, Fig. S10A; constituent → serum → module Sankey diagram, Fig. S10B). The in-blood fraction thus intersects the same transcriptional modules that the

single-cell analysis identified as altered, which is how the formulation is linked to the immune axis examined here; the serum metabolome otherwise differed only marginally from Control. Because no porcine component–target database exists (Zheng et al. 2024), targets were predicted from human resources (SwissTargetPrediction, TCMSP), ortholog-mapped to Sus scrofa via UniProt/Ensembl, and intersected with the porcine DEG set; 'convergence' therefore denotes co-occurrence within shared transcriptional modules, not demonstrated binding, target engagement or causality, and circulating concentrations were not determined.

APRR reshapes the neutrophil-centered communication circuit without restoring the T-cell effector state

CellChat inferred the global ligand–receptor network across the three groups (Fig. 6A–D); by-group differential analysis indicated that APRR partially restored most PRRSV-suppressed pathways toward the Control state. Neutrophil-centered MIF signaling was strong in PRRSV and receded under APRR (Fig. S5A), and the PD-1/PD-L1 focus mirrored the attenuation in Fig. 5 (Fig. S5B). APRR therefore rewired the communication network rather than uniformly suppressing it.

At the effector level, rescue was incomplete. APRR neutrophils were the most activated of the three groups, marginally above PRRSV (Δmean $\approx$ 0.07 z; $p = 2.6\times10^{-3}$, within-sample and not a between-animal test) and well above Control ($p < 1\times10^{-15}$). Their inflammatory profile shifted from PRRSV's CXCL8-driven signature toward an S100A8 / CCL2 / IL1B / IL6-driven one (Fig. 6E–H). The sixteen neutrophil activation states and their 11-marker signature (MPO, CXCL8, S100A8, S100A9, CSF3R, CXCR2, IL1B, CCL2, TNF, IL6, LCN2; FCGR3B not detected in this subset and excluded) are defined in Fig. 6E–F, with activation score and state composition in Fig. 6G–H.

T cells, in contrast, showed no reversal of exhaustion: the APRR exhaustion score (0.249) was indistinguishable from PRRSV (0.256), and the PD-1 / TIM-3 / LAG3 / TIGIT / CTLA4 program was not reversed (Fig. 6I–L). The eleven T-cell states and their 20-marker signature (CD3E, CD8A, CD4, CCR7, IL7R, FOXP3, GZMK, GZMB, PRF1, IFNG, NKG7, GNLY, CD69, PDCD1, LAG3, HAVCR2, CTLA4, TIGIT, TNFRSF9, ENTPD1) are defined in Fig. 6I–J, with exhaustion score and state composition in Fig. 6K–L. Communication remodeling and effector-cell rescue thus diverge: APRR partly normalizes cell–cell signaling and checkpoint ligand expression without achieving full functional immune restoration, consistent with the persistent T-cell exhaustion in Fig. 4.

CellChat and ligand–target scoring converge on a neutrophil-centered communication circuit that APRR attenuates. The circuit spans MIF / PD-L1 communication, activation-state shifts and ligand-driven programming, placing APRR's effect upstream of the neutrophil state rather than only within it. Supporting outputs are in Fig. S5 (focused CellChat views) and Fig. S6 (top ligand–receptor pairs, pathway enrichment and ISG boxplots, the latter corroborating the interferon rescue in Fig. S2); ssGSEA pathway activity is in Fig. S9, together with per-cell-type KEGG enrichment resolving cytokine–receptor interaction, PD-L1/PD-1 checkpoint signaling, antigen processing and interferon-related terms, with inflammatory and interferon programs receding under APRR.

Discussion

In PRRSV-challenged pigs, dietary APRR reduced lung and spleen viral RNA and lowered clinical scores, and lung single-cell profiles from the same animals showed a parallel shift in the immune compartment. The largest compositional change was an expanded neutrophil population carrying a PD-L1-associated program. That population was smaller in APRR-treated pigs, whereas the PD-L1 program score measured within the remaining pdl1^{+} cells was not reduced (Fig. 3B, C, E). T-cell composition and inferred intercellular signaling moved the same way, and neither returned to the Control pattern.

Neutrophils are functionally heterogeneous, and subsets that suppress lymphocyte responses have been described in viral infection and in tumors (Johansson and Kirsebom 2021; Palomino-Segura et al. 2023; Zhang et al. 2024). Excessive neutrophil activation and extracellular trap release aggravate lung injury, whereas granulocytic suppressor phenotypes restrain T-cell responses (Pan and Lee 2024). PRRSV infection delays virus-specific cellular immunity and perturbs the pulmonary immune compartment (Cai et al. 2023; Fiers et al. 2024), and a PD-L1-associated neutrophil population with comparable properties has been reported in HIV infection (Madzime et al. 2021). The population described here offers a candidate cellular basis for the impaired T-cell responses seen in infected lung.

In the T-cell compartment, infection shifted CD4^{+}:CD8^{+} proportions and reduced effector transcripts, and APRR partially reversed both (Fig. 4). Recovery was uneven at the gene level. GNLY rose above the Control value, IL7R and CD44 returned toward or above Control, TCF7 and CCR7 increased but stayed below Control, and PRF1 and GZMK were lower under APRR than under PRRSV (Fig. 4E). Checkpoint transcripts behaved differently again: PDCD1 and CTLA4 were unchanged, while LAG3, TIGIT and HAVCR2 remained above the Control level and were numerically higher than in the PRRSV group. The per-cell exhaustion score did not fall under APRR (Fig. 6K), so the response is best described as partial restoration of effector transcripts without reversal of the exhaustion program.

CellChat predicted weaker PD-L1/PD-1 signaling from neutrophils to CD4^{+} T cells in APRR-treated lungs (Fig. 5B and Fig. 6), as would be expected if fewer PD-L1-high neutrophils were available to engage PD-1 on neighboring T cells. Lung tissue-resident memory T cells are positioned for such neutrophil–T-cell contact (Carbone 2022; Zheng and Wakim 2022), and neutrophil–T-cell crosstalk is an established determinant of adaptive outcomes (Madzime et al. 2021); PD-L1/PD-1 signaling restrains T-cell activation in both tumor and infection settings (Sun et al. 2018; Yamaguchi et al. 2022). Delayed and suboptimal virus-specific T-cell responses are well documented in PRRSV infection, and PD-L1-mediated suppression is a plausible contributor (Cai et al. 2023; Fiers et al. 2024). The present data are correlative on this point: they show that the predicted interaction weakened in parallel with the neutrophil shift, not that the interaction caused the T-cell phenotype.

SCENIC, run with human (hg38) cisTarget rankings because no porcine ranking is available, nominated IRF1 and STAT1 as regulons enriched in the neutrophil compartment and attenuated under APRR. Conservation of cis-regulatory elements between human and pig is limited, so these are cross-species inferences that require porcine-specific validation. Both factors have been linked to PD-L1 regulation

(Yamaguchi et al. 2022), but the present data do not show that they act on CD274 directly; they identify candidate components of the transcriptional program that accompanies PRRSV-associated neutrophil activation and is attenuated after APRR treatment.

The neutrophil expansion described here is not specific to PRRSV. Comparable states appear in influenza and respiratory syncytial virus infection (Johansson and Kirsebom 2021; Zhang et al. 2024), and COVID-19 lung atlases have resolved neutrophil states that combine inflammatory and immunoregulatory programs (Sikkema et al. 2023). What matters more for pig health is the consequence: PRRSV-induced immunosuppression predisposes to co-infection within the porcine respiratory disease complex (Chen et al. 2023; Fiers et al. 2024; Jian et al. 2022), and PRRSV impairs macrophage phagolysosomal killing, which facilitates secondary bacterial infection (Duan et al. 2025). If APRR reduces the abundance of PD-L1-high neutrophils, that effect would act alongside direct antiviral activity, but the present data do not test whether it lowers secondary infection rates.

An independent network-pharmacology analysis linked a small set of in-blood APRR constituents to the same core nodes (TNF, PD-L1) that the single-cell data surfaced (Fig. S10), which supplies a testable chemical entry point for the neutrophil phenotype rather than a generic multi-component claim.

APRR reduced viral titer, N protein and ORF7 RNA in Marc-145 cells along a dose-dependent gradient, reaching a 2.8-log reduction in TCID50 at the highest concentration tested. Several constituent classes annotated by HPLC-MS have documented antiviral or anti-inflammatory activity, including glycyrrhizin (Huan et al. 2021), cryptotanshinone (Li et al. 2021) and chlorogenic acid (Huang et al. 2023). None of the three is among the 111 serum-detectable constituents: glycyrrhizin, cryptotanshinone and chlorogenic acid rank 16th, 371st and 775th by abundance among the 1,198 annotated constituents. The in-blood fraction is instead dominated by baicalin (24.5% of in-blood signal) and oleamide (25.3%); oleamide is a putatively endogenous long-chain fatty amide whose serum signal cannot be attributed to the formula without targeted quantification. Baicalin suppresses NLRP3 inflammasome and NF-κB signaling in porcine immune cells (Fang et al. 2020; Fu et al. 2016), which is consistent with the lower serum IL-1β and reduced lung p-p65 observed here (Fig. 5I, J).

A 2.8-log in vitro effect does not by itself explain the in vivo phenotype, which included changes in immune cell states and in inferred intercellular communication at exposures that were not quantified. Multi-component herbal formulations are usually evaluated as polypharmacological interventions, and network pharmacology links constituents to multiple host targets (Zheng et al. 2024). Type I interferon induction suppresses PRRSV replication (Chang et al. 2024b), and the ISG program recovered in APRR-treated lungs is consistent with that route, which is one of the four measured pillars. We therefore interpret APRR as acting through both direct antiviral and host-directed components, without being able to partition their relative contributions.

The IL1R2 step is the largest gap in the model. IL1R2 protein could not be measured because no sample material remained after the analyses reported here, so the ordering IL1R2↑ → attenuated IL-1β signaling → NF-κB↓ remains correlative at its first step. The downstream steps have independent support from

lung p-p65 immunofluorescence (Fig. 5I) and serum IL-1β ELISA (Fig. 5J). The PD-L1–T-cell interaction is correlative in the same way: PD-L1 protein was not localized to neutrophils in situ, and suppression of $CD4^+$ T cells by this population was not tested functionally. T-cell effector recovery is transcript-level only and was not confirmed by restimulation or intracellular cytokine staining. Reduced IL-1β protein is also not uniquely explained by IL1R2 induction: APRR constituents could dampen NLRP3 activation, suppress IL1B transcription or caspase-1-dependent maturation, or alter cytokine stability. The design cannot distinguish among these routes, and the dashed arrow with a question mark in Fig. 5G marks that inference.

Scope and inferential limits. Each group is represented by a single animal, so the single-cell comparisons are exploratory point estimates rather than population-level tests; cell-level P values describe within-sample heterogeneity and cannot be read as evidence of a treatment effect across animals. The single-cell findings, including the IL1R2↑ → IL-1β↓ → NF-κB↓ ordering, the PD-L1 program and the inferred ligand–receptor interactions, are therefore hypothesis-generating and motivate confirmatory work with independent biological replicates. Ligand-target ranking came from a curated scoring scheme rather than an unbiased prior-based model, so the order of candidate ligands is a prioritization of hypotheses, not a quantitative measure of ligand activity. Group comparisons in the Results are reported as descriptive cell-level differences for the same reason. Sampling was also restricted to a single post-challenge time point (10 d), so neither earlier nor later phases of the neutrophil and T-cell response were profiled.

Bridging the in vitro and in vivo exposure. The in vitro work used a decoction extract, whereas pigs received APRR powder in feed, so the two preparations differ in composition, bioavailability and effective exposure. Of the 111 constituents detected in serum, 23 changed significantly relative to control pigs (FDR < 0.05) and 88 could not be distinguished from endogenous background; absolute circulating concentrations were not determined (Materials and methods). A quantitative bridge between active in vitro concentrations and in vivo exposure is therefore unavailable, and the in vitro dose–response should not be read as an explanation of the in vivo phenotype. The dietary level of 4 kg/t is the field application dose rather than an experimentally optimized one, so the data do not locate this level on an exposure–response curve. Because the prototypes that account for the in vitro activity are not among the serum-detectable constituents, the in vivo effect cannot be attributed to the same molecules; the two arms of the study probe related but not identical chemical exposures.

Proposed validation roadmap. Four experiments would turn the present model into a demonstrated mechanism: (i) flow cytometry or multiplex immunofluorescence to localize PD-L1 protein on lung neutrophils in situ; (ii) co-culture of sorted pulmonary neutrophils with autologous T cells, with and without anti-PD-L1 blockade, read out by CFSE dilution and IFN-γ/IL-2 production; (iii) in vivo PD-L1 blockade, or myeloid-restricted CD274 deletion, during challenge to test causality; and (iv) scRNA-seq with at least three animals per group to permit between-animal inference.

Effector recovery without exhaustion reversal: a progenitor-like state? The dissociation between effector-transcript recovery and persistent exhaustion is informative rather than anomalous. In chronic viral infection and cancer, TCF1^{+} (TCF7^{+}) PD-1^{+} cells form a progenitor exhausted pool that retains proliferative capacity, whereas terminally exhausted cells are epigenetically fixed through TOX-dependent chromatin remodeling. The APRR profile, with higher IL7R and CD44 and partially higher TCF7 and CCR7 alongside unchanged PDCD1 and CTLA4, is compatible with a shift toward such a state, but the concurrent rise in LAG3, TIGIT and HAVCR2 argues against simple re-differentiation. We present this as one interpretation of the transcriptional data. Testing it would require ATAC-seq and antigen-specific restimulation with intracellular cytokine readouts, both beyond the present scope; better recall responsiveness on re-exposure is the prediction that follows, and it remains untested.

PRRSV infection expands PD-L1-associated neutrophil states and remodels T-cell composition and intercellular communication, and APRR attenuates each of these features. Neutrophil-centered immune regulation is a candidate axis in PRRSV pathogenesis; the roadmap above defines the experiments that would test it, and baicalin is the most concrete chemical entry point among the in-blood constituents.

APRR, a chemically defined multi-component herbal formulation, inhibited PRRSV replication in Marc-145 cells and reduced lung and spleen viral RNA, clinical scores and rectal temperature in a pig challenge model. Lung single-cell profiling identified an expanded, PD-L1-associated neutrophil population in infected pigs that was smaller after APRR treatment, together with partial recovery of T-cell effector transcripts and weaker inferred neutrophil-to-T-cell PD-L1 signaling. These changes are consistent with the four-pillar working model: PD-L1 downregulation, IL-1β protein reduction, ISG antiviral-axis rebuilding, and neutrophil-infiltration reversal. Two downstream readouts of that axis, serum IL-1β and lung p-p65, were reduced at the protein level. APRR did not normalize neutrophil activation or reverse T-cell exhaustion, so the response is a partial restoration of specific pathways rather than general immune reconstitution; the roadmap above sets out the experiments that would test causality.

Abbreviations

APRR
Anti-PRRSV Prescription of Radix et Rhizoma (multi-component herbal formulation)
PRRSV
porcine reproductive and respiratory syndrome virus
scRNA-seq
single-cell RNA sequencing
DEG
differentially expressed gene
ISG
interferon-stimulated gene
IF
immunofluorescence

ELISA
enzyme-linked immunosorbent assay
NF-κB
nuclear factor kappa B
p-p65
phosphorylated p65 (NF-κB subunit)
PD-1
programmed cell death protein 1
PD-L1
programmed death-ligand 1
TCID50
50% tissue culture infectious dose
GSA
Genome Sequence Archive
HPLC-MS
high-performance liquid chromatography-mass spectrometry
KEGG
Kyoto Encyclopedia of Genes and Genomes
ssGSEA
single-sample gene set enrichment analysis
UMAP
uniform manifold approximation and projection
QC
quality control
ANOVA
analysis of variance
SD
standard deviation
PBS
phosphate-buffered saline
FBS
fetal bovine serum
DMEM
Dulbecco's modified Eagle medium
CCK-8
Cell Counting Kit-8
BSA
bovine serum albumin
SDS-PAGE
sodium dodecyl sulfate–polyacrylamide gel electrophoresis

PCA
principal component analysis
FDR
false discovery rate.

Declarations

Statement of Animal Ethics

All animal experiments were approved by the Institutional Animal Care and Use Committee (IACUC) of Huazhong Agricultural University (approval no. HZAUSW-2025-0110) and were conducted in accordance with institutional guidelines and the ARRIVE (Animal Research: Reporting of In Vivo Experiments) guidelines. No human participants or human-derived material were involved, so consent to participate was not required.

Conflict of Interest Statement

F.Z. is affiliated with Fujian Aonong Biological Technology Group Incorporation Limited and participated in the experimental design; the remaining authors declare no competing interests.

Consent for publication

Not applicable.

Competing interests

F.Z. is affiliated with Fujian Aonong Biological Technology Group Incorporation Limited and participated in the experimental design; the remaining authors declare no competing interests. The authors have no other relevant financial or non-financial interests to disclose.

Consent to participate

Not applicable. No human participants or human-derived material were involved, so consent to participate was not required.

Funding

This work was supported by the Innovative Job Funds of Agricultural Science and Technology of Hubei Province (Grant No. 2026-620-000-001-026).

Author Contribution

Y.X. conceived the project and designed the experiments; F.Z. participated in the experimental design. Y.X. supervised the project and obtained funding. J.P. and X.W. performed all the experiments, analyzed the data and wrote the manuscript. W.Z., X.F., D.C., S.L., P.C., H.D., D.S. and Z.Z. discussed the results and critically reviewed the manuscript. All the authors revised the manuscript and approved the submitted version.

Acknowledgements

Not applicable.

Data Availability

The raw sequencing data of scRNA-seq reported in this paper have been deposited in the Genome Sequence Archive of the National Genomics Data Center under accession number PRJCA065583. Data access is currently controlled; researchers may apply for access via the Data Access Committee link on the accession page. The datasets and source codes generated in this study can be found in online repositories (GitHub: https://github.com/jintaopeng1121-netizen/Sscrofa_data); further materials are available from the corresponding author on reasonable request.

References

1. Aibar S, González-Blas CB, Moerman T et al (2017) SCENIC: single-cell regulatory network inference and clustering. Nat Methods 14:1083–1086. https://doi.org/10.1038/nmeth.4463
2. Bello-Onaghise G, Wang G, Han X, Nsabimana E, Cui W, Yu F et al (2020) Antiviral strategies of Chinese herbal medicine against PRRSV infection. Front Microbiol 11:1756. https://doi.org/10.3389/fmicb.2020.01756
3. Bert S, Nadkarni S, Perretti M (2023) Neutrophil-T cell crosstalk and the control of the host inflammatory response. Immunol Rev 314:36–49. https://doi.org/10.1111/imr.13162
4. Bravo González-Blas C, De Winter S, Hulselmans G, Hecker N, Matetovici I, Christiaens V et al (2023) SCENIC+: single-cell multiomic inference of enhancers and gene regulatory networks. Nat Methods 20:1355–1367. https://doi.org/10.1038/s41592-023-01938-4
5. Burn G, Foti A, Marsman G, Patel D, Zychlinsky A (2021) The neutrophil. Immunity 54:1377–1391. https://doi.org/10.1016/j.immuni.2021.06.006

6. Cai H, Zhang H, Cheng H, Liu M, Wen S, Ren J (2023) Progress in PRRSV infection and adaptive immune response mechanisms. Viruses 15:1442. https://doi.org/10.3390/v15071442
7. Carbone F (2022) Unique properties of tissue-resident memory T cells in the lungs. Nat Rev Immunol 23:329–335. https://doi.org/10.1038/s41577-022-00815-z
8. Castanheira F, Kubes P (2019) Neutrophils and NETs in modulating acute and chronic inflammation. Blood 133:2178–2185. https://doi.org/10.1182/blood-2018-11-844530
9. Chang X, Ma J, Zhou Y, Xiao S, Xiao X, Fang L (2024a) Development of a ferritin protein nanoparticle vaccine with PRRSV GP5 protein. Viruses 16:991. https://doi.org/10.3390/v16060991
10. Chang X, Wang M, Li Z, Wang L, Zhang G, Chang Y et al (2024b) FADD promotes type I interferon production to suppress porcine reproductive and respiratory syndrome virus infection. Front Vet Sci 11:1380144. https://doi.org/10.3389/fvets.2024.1380144
11. Chen X, Qiao S, Li R, Wang J, Li X, Zhang G (2023) Evasion strategies of porcine reproductive and respiratory syndrome virus. Front Microbiol 14:1140449. https://doi.org/10.3389/fmicb.2023.1140449
12. Cheng J, Sun N, Zhao X, Niu L, Song M, Sun Y, Jiang J, Guo J, Bai Y, He J, Li H (2013) In vitro screening for compounds derived from traditional Chinese medicines with antiviral activities against porcine reproductive and respiratory syndrome virus. J Microbiol Biotechnol 23:1076–1083. https://doi.org/10.4014/jmb.1303.03074
13. Duan E, Wang D, Fang L, Ma J, Luo J, Chen H, Li K, Xiao S (2015) Suppression of porcine reproductive and respiratory syndrome virus proliferation by glycyrrhizin. Antiviral Res 122:31–37. https://doi.org/10.1016/j.antiviral.2015.06.001
14. Duan D, Cao C, Qiu L, Li X, Chen H (2025) Paradigm shift: PRRSV-mediated active remodeling of the host immune system – From epigenetic domestication to functional hijacking. Front Microbiol 16:1738504. https://doi.org/10.3389/fmicb.2025.1738504
15. Fang F, Xie Z, Quan J, Wei X, Wang L, Yang L (2020) Baicalin suppresses Propionibacterium acnes-induced skin inflammation by downregulating the NF-κB/MAPK signaling pathway and inhibiting activation of NLRP3 inflammasome. Braz J Med Biol Res 53:e9949. https://doi.org/10.1590/1414-431X20209949
16. Fiers J, Cay A, Maes D, Tignon M (2024) A comprehensive review on porcine reproductive and respiratory syndrome virus with emphasis on immunity. Vaccines 12:942. https://doi.org/10.3390/vaccines12080942
17. Fu S, Xu L, Li S, Qiu Y, Liu Y, Wu Z, Ye C, Hou Y, Hu CA (2016) Baicalin suppresses NLRP3 inflammasome and nuclear factor-kappa B (NF-κB) signaling during Haemophilus parasuis infection. Vet Res 47:80. https://doi.org/10.1186/s13567-016-0359-4
18. Garlanda C, Dinarello CA, Mantovani A (2013) The interleukin-1 family: back to the future. Immunity 39:1003–1018. https://doi.org/10.1016/j.immuni.2013.11.010
19. Hao Y, Hao S, Andersen-Nissen E, Mauck W, Zheng S, Butler A et al (2021) Integrated analysis of multimodal single-cell data. Cell 184:3573–3587e29. https://doi.org/10.1016/j.cell.2021.04.048

20. Hao Y, Stuart T, Kowalski M, Choudhary S, Hoffman P, Hartman A et al (2024) Dictionary learning for integrative, multimodal and scalable single-cell analysis. Nat Biotechnol 42:293–304. https://doi.org/10.1038/s41587-023-01767-y
21. He Z, Yan J, Liu M, Liao J, Li F, Guo C (2025) Host innate immune antagonism and immune evasion strategies of porcine reproductive and respiratory syndrome virus. Int J Biol Macromol 322:146756. https://doi.org/10.1016/j.ijbiomac.2025.146756
22. Heumos L, Schaar A, Lance C, Litinetskaya A, Drost F, Zappia L et al (2023) Best practices for single-cell analysis across modalities. Nat Rev Genet 24:550–572. https://doi.org/10.1038/s41576-023-00586-w
23. Hu A, Guo Y, Zhou Y, Chen P, Zhu Y, Liu T et al (2025) Single-cell RNA sequencing analysis reveals a novel porcine alveolar macrophage subtype with high SLAMF7 expression promoting PRRSV infection. Virulence 16:2560894. https://doi.org/10.1080/21505594.2025.2560894
24. Huan C, Xu Y, Zhang W, Guo T, Pan H, Gao S (2021) Research progress on the antiviral activity of glycyrrhizin. Front Pharmacol 12:680674. https://doi.org/10.3389/fphar.2021.680674
25. Huang C, Zhu J, Wang L, Chu A, Yin Y, Vali K, Garmendia A, Tang Y (2020) Cryptotanshinone protects porcine alveolar macrophages from infection with porcine reproductive and respiratory syndrome virus. Antiviral Res 183:104937. https://doi.org/10.1016/j.antiviral.2020.104937
26. Huang K, Zhang P, Zhang Z, Youn J, Wang C, Zhang H et al (2021) TCM in the treatment of COVID-19 and other viral infections. Pharmacol Ther 225:107843. https://doi.org/10.1016/j.pharmthera.2021.107843
27. Huang J, Xie M, He L, Song X, Cao T (2023) Chlorogenic acid: a review on its mechanisms of anti-inflammation. Front Pharmacol 14:1218015. https://doi.org/10.3389/fphar.2023.1218015
28. Jian Z, Ma R, Zhu L, Deng H, Li F, Zhao J et al (2022) Evasion of interferon-mediated immune response by arteriviruses. Front Immunol 13:963923. https://doi.org/10.3389/fimmu.2022.963923
29. Jin S, Guerrero-Juarez C, Zhang L, Chang I, Ramos R, Kuan C et al (2021) Inference and analysis of cell-cell communication using CellChat. Nat Commun 12:1088. https://doi.org/10.1038/s41467-021-21246-9
30. Johansson C, Kirsebom F (2021) Neutrophils in respiratory viral infections. Mucosal Immunol 14:815–827. https://doi.org/10.1038/s41385-021-00397-4
31. Jovic D, Liang X, Zeng H, Lin L, Xu F, Luo Y (2022) Single-cell RNA sequencing technologies and applications. Clin Transl Med 12:e694. https://doi.org/10.1002/ctm2.694
32. Kazer S, Aicher T, Muema D, Carroll S, Ordovas-Montanes J, Miao V et al (2020) Integrated single-cell analysis of multicellular immune dynamics during hyperacute HIV-1 infection. Nat Med 26:511–518. https://doi.org/10.1038/s41591-020-0799-2
33. Kim S, Kim H, Kang S, Rasool A, Ryu J, Lee J et al (2025) The role of immune checkpoint molecules in PRRSV-2-induced immune modulation: insights from comparative in vivo evaluation including NADC34-like PRRSV. J Virol 99:e02298–e02224. https://doi.org/10.1128/jvi.02298-24

34. Li H, Gao C, Liu C, Liu L, Zhuang J, Yang J et al (2021) A review of the biological activity and pharmacology of cryptotanshinone. Biomed Pharmacother 137:111332. https://doi.org/10.1016/j.biopha.2021.111332
35. Li J, Miller LC, Sang Y (2024) Current status of vaccines for PRRS. Vaccines 12:606. https://doi.org/10.3390/vaccines12060606
36. Li J, Liang Y, Zhang Y, Xu Y, Liu F, Ding L et al (2026) Deciphering immune features and cellular heterogeneity in PRRSV infection via single-cell RNA sequencing. J Virol 100:e01828–e01825. https://doi.org/10.1128/jvi.01828-25
37. Lim B, Kim S, Kim H, Kim J, Seo Y, Lim C et al (2025) Single-cell transcriptomics of bronchoalveolar lavage during PRRSV infection with different virulence. Nat Commun 16:1112. https://doi.org/10.1038/s41467-024-54676-2
38. Liu G, Huang X, Yang Y, Chen M, Tian X, Song H et al (2025) GP2a I118 and GP4 D43 play critical roles in the attachment of PRRSV to the CD163 receptor: implications for anti-PRRSV infection targets. J Virol 99:e00963–e00925. https://doi.org/10.1128/jvi.00963-25
39. Madzime M, Rossouw T, Theron A, Anderson R, Steel H (2021) Interactions of HIV and antiretroviral therapy with neutrophils and platelets. Front Immunol 12:634386. https://doi.org/10.3389/fimmu.2021.634386
40. McGinnis C, Murrow L, Gartner Z (2019) DoubletFinder: doublet detection in single-cell RNA sequencing data using artificial nearest neighbors. Cell Syst 8:329–337. https://doi.org/10.1016/j.cels.2019.03.003
41. McMahan CJ, Slack JL, Mosley B, Cosman D, Lupton SD, Brunton LL et al (1991) A novel IL-1 receptor, cloned from B cells by mammalian expression, is expressed in many cell types. EMBO J 10:2821–2832. https://doi.org/10.1002/j.1460-2075.1991.tb07831.x
42. Palomino-Segura M, Sicilia J, Ballesteros I, Hidalgo A (2023) Strategies of neutrophil diversification. Nat Immunol 24:575–584. https://doi.org/10.1038/s41590-023-01452-x
43. Pan T, Lee J (2024) A crucial role of neutrophil extracellular traps in pulmonary infectious diseases. Chin Med J Pulm Crit Care Med 2:34–41. https://doi.org/10.1016/j.pccm.2023.10.004
44. Reed L, Muench H (1938) A simple method of estimating fifty per cent endpoints. Am J Epidemiol 27:493–497. https://doi.org/10.1093/oxfordjournals.aje.a118408
45. Ribeiro G, de Souza E, Palmisano G, Durigon E, Liebau E, Wrenger C (2025) Plant-derived extracts and natural products with antiviral activity. Front Virol 5:1632734. https://doi.org/10.3389/fviro.2025.1632734
46. Rowland R, Brandariz-Nuñez A (2024) Role of CD163 in PRRSV infection. Virology 600:110262. https://doi.org/10.1016/j.virol.2024.110262
47. Ruedas-Torres I, Sánchez-Carvajal J, Carrasco L, Pallarés F, Larenas-Muñoz F, Rodríguez-Gómez I et al (2023) PRRSV-1 induced lung lesion is associated with an imbalance between costimulatory and coinhibitory immune checkpoints. Front Microbiol 13:1007523. https://doi.org/10.3389/fmicb.2022.1007523

48. Salzmann M, Gibler P, Haider P, Brekalo M, Plasenzotti R, Filip T et al (2024) Neutrophil extracellular traps induce persistent lung tissue damage via thromboinflammation without altering virus resolution in a mouse coronavirus model. J Thromb Haemost 22:188–198. https://doi.org/10.1016/j.jtha.2023.09.014
49. Sikkema L, Ramírez-Suástegui C, Strobl D, Gillett T, Zappia L, Madissoon E et al (2023) An integrated cell atlas of the lung in health and disease. Nat Med 29:1563–1577. https://doi.org/10.1038/s41591-023-02327-2
50. Sun C, Mezzadra R, Schumacher T (2018) Regulation and function of the PD-L1 checkpoint. Immunity 48:434–452. https://doi.org/10.1016/j.immuni.2018.03.014
51. Wu T, Hu E, Xu S, Chen M, Guo P, Dai Z et al (2021) clusterProfiler 4.0. Innovation (Camb) 2:100141. https://doi.org/10.1016/j.xinn.2021.100141
52. Xuan N, Zhao J, Kang Z, Cui W, Tian B (2024) Neutrophil extracellular traps and their implications in airway inflammatory diseases. Front Med 10:1331000. https://doi.org/10.3389/fmed.2023.1331000
53. Yamaguchi H, Hsu J, Yang W, Hung M (2022) Mechanisms regulating PD-L1 expression. Nat Rev Clin Oncol 19:287–305. https://doi.org/10.1038/s41571-022-00601-9
54. Zhang X, Guo C (2022) Recent advances in inhibition of porcine reproductive and respiratory syndrome virus through targeting CD163. Front Microbiol 13:1006464. https://doi.org/10.3389/fmicb.2022.1006464
55. Zhang Z, Li Z, Li H, Yang S, Ren F, Bian T et al (2022) The economic impact of PRRS outbreak in four Chinese farms. Front Vet Sci 9:1024720. https://doi.org/10.3389/fvets.2022.1024720
56. Zhang F, Xia Y, Su J, Quan F, Zhou H, Li Q et al (2024) Neutrophil diversity and function in health and disease. Signal Transduct Target Ther 9:349. https://doi.org/10.1038/s41392-024-02049-y
57. Zheng M, Wakim L (2022) Tissue resident memory T cells in the respiratory tract. Mucosal Immunol 15:379–388. https://doi.org/10.1038/s41385-021-00461-z
58. Zheng S, Liang Y, Xue T, Wang W, Li S, Zhang P et al (2024) Application of network pharmacology in traditional Chinese medicine for the treatment of digestive system diseases. Front Pharmacol 15:1412997. https://doi.org/10.3389/fphar.2024.1412997

Figures

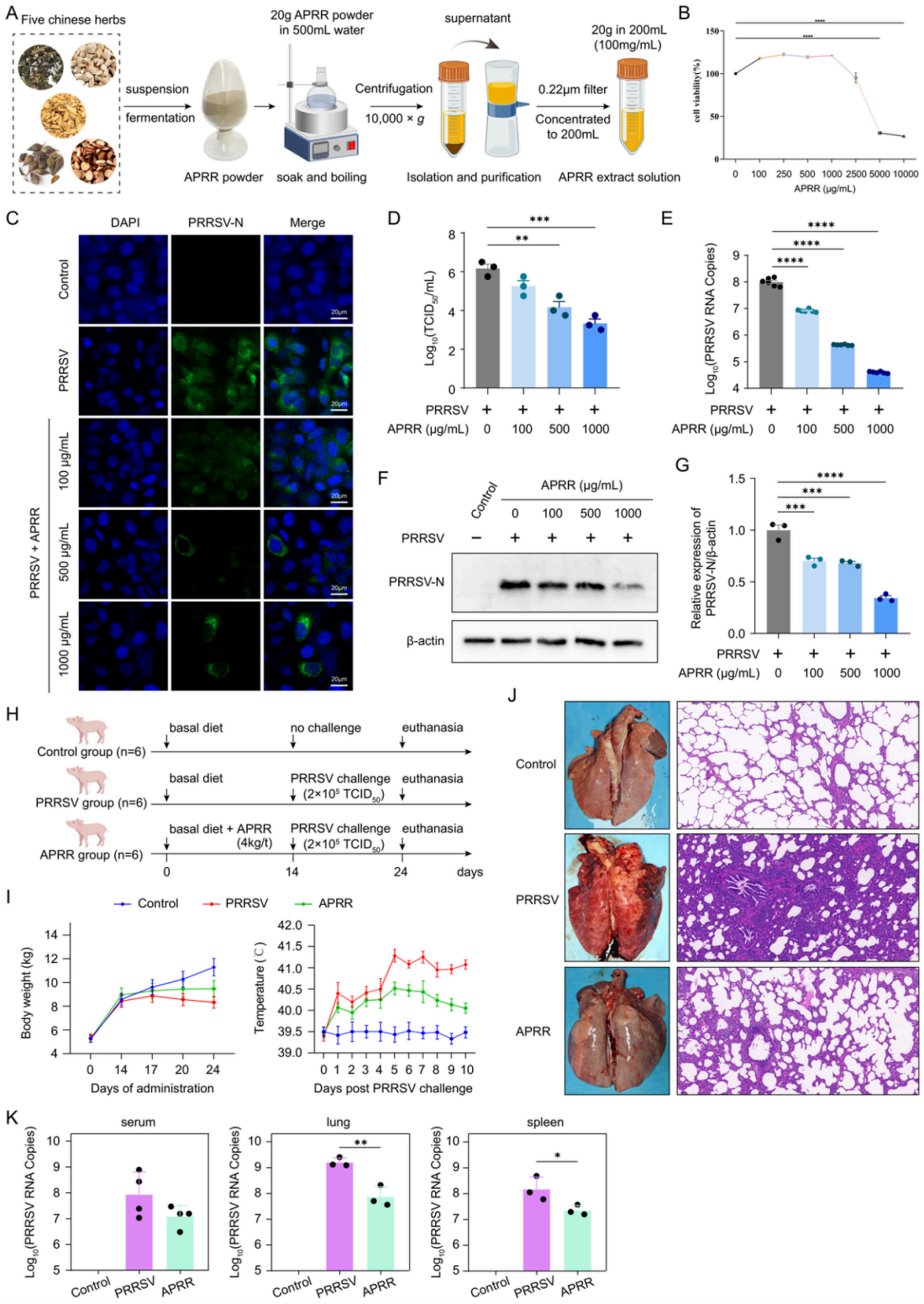


Figure 1

APRR suppresses PRRSV replication in vitro and attenuates PRRSV-induced disease in vivo. (A) APRR preparation workflow. (B) CCK-8 cell-viability of Marc-145 cells. (C) Triple-channel immunofluorescence for PRRSV-N. (D) Viral titer bar plot (log10 TCID50/mL). (E) Log10(PRRSV ORF7 RNA copies) qRT-PCR bar plot. (F) PRRSV-N Western blot with β-actin loading control. (G) Densitometric quantification of PRRSV-N. (H) In vivo challenge-study design. (I) Body-weight and rectal-temperature trajectories. (J)

Gross lung morphology and H&E staining (Control, PRRSV and APRR). (K) Viral RNA loads in serum, lung and spleen (serum, log10 copies per mL; tissue, log10 copies per g); APRR reduced viral RNA in lung and spleen, with a smaller decrease in serum that did not reach significance (values in Results)

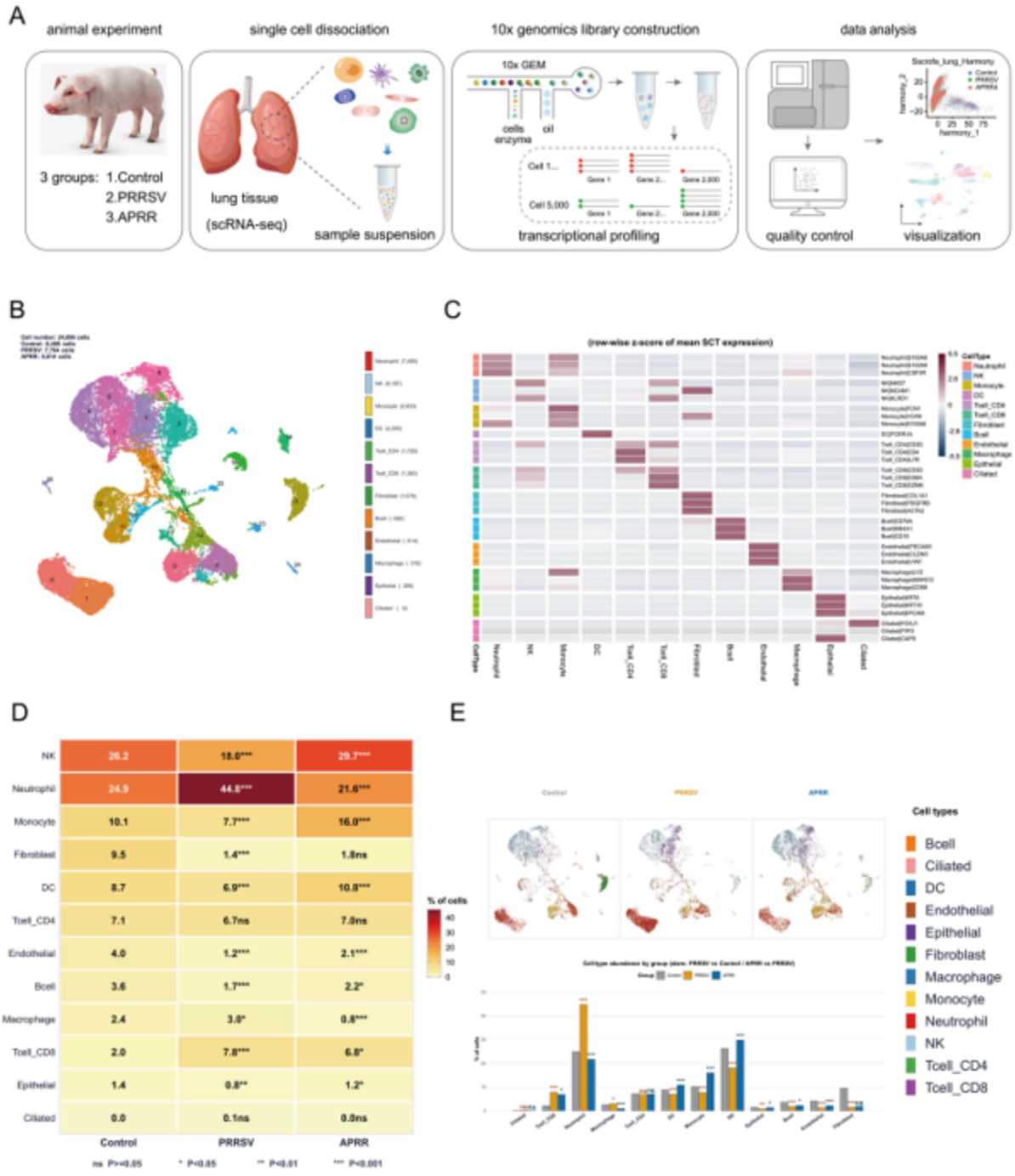


Figure 2

Single-cell landscape of the PRRSV-infected lung. (A) scRNA-seq workflow. (B) UMAP of all 24,896 cells (8,488 Control / 7,794 PRRSV / 8,614 APRR) across twelve cell types. (C) Marker-gene heat map of the twelve cell-type annotations. (D) Cell-type composition heat map by group. (E) Top-shifted cell populations across groups

Per-group UMAPs recovered the same major cell types in all three groups (Fig. S1A–C). Features and counts per cell were balanced across groups (Fig. S1D, E), and removal of doublets with DoubletFinder left a low, balanced doublet rate across groups and samples (Fig. S1F–H).

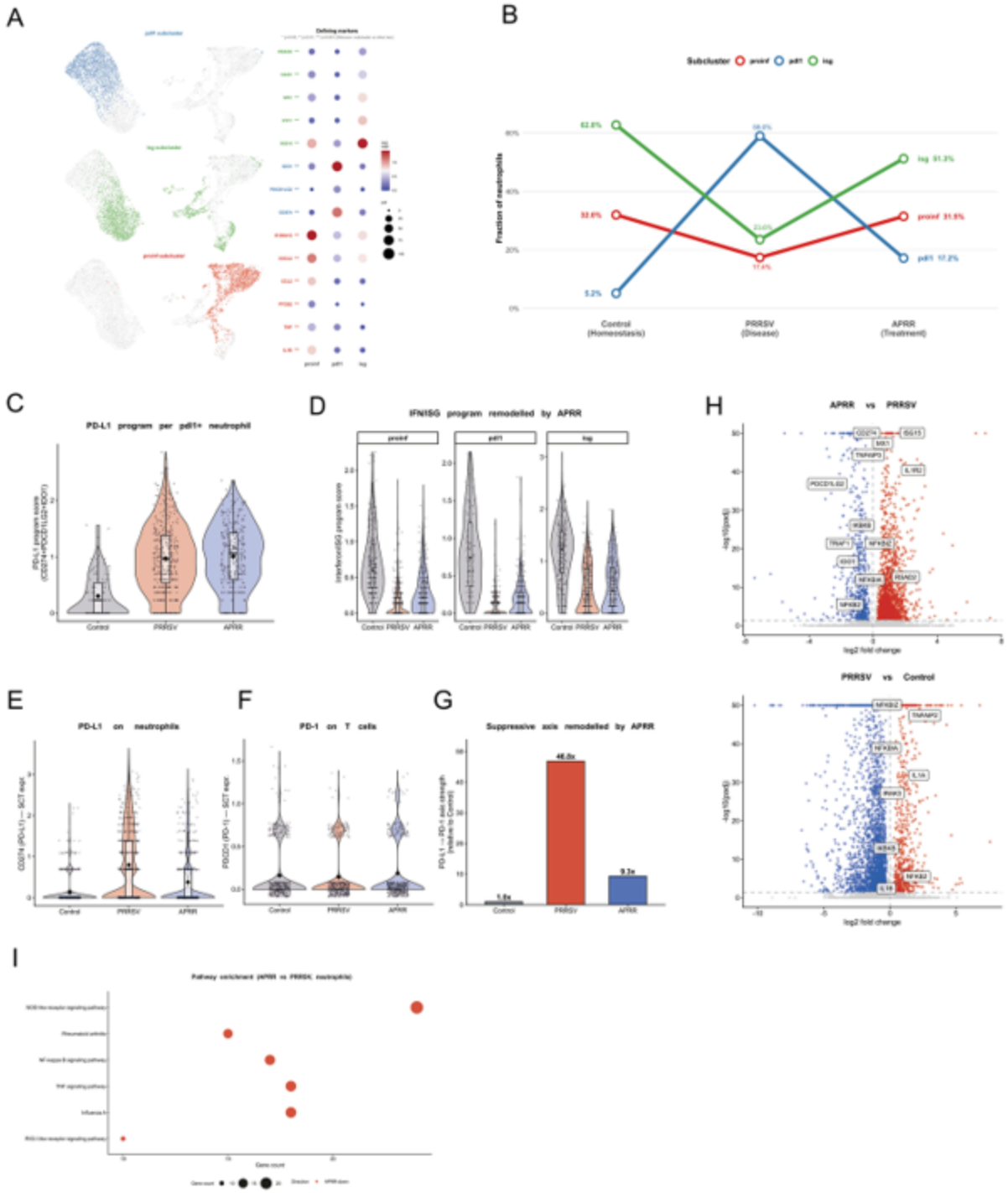


Figure 3

APRR remodels neutrophil states and lowers PD-L1 burden on the neutrophil compartment. Neutrophils resolved into three functional subclusters (proinf, pdl1 and isg) defined by state-specific markers (A). Compositional shift across groups (B). PD-L1 program score per pdl1⁺ neutrophil (C). IFN/ISG program scores under APRR (D). PD-L1 (CD274) on neutrophils (E) and PD-1 (PDCD1) on T cells (F). PD-L1→PD-1

axis-strength index (pdl1⁺ neutrophil abundance × per-cell CD274 × T-cell PD-1, normalized to Control) across groups (G). Dual volcano of APRR- vs PRRSV (top) and PRRSV- vs Control (bottom) neutrophil DEGs (H). KEGG enrichment of APRR-altered neutrophil DEGs (I)

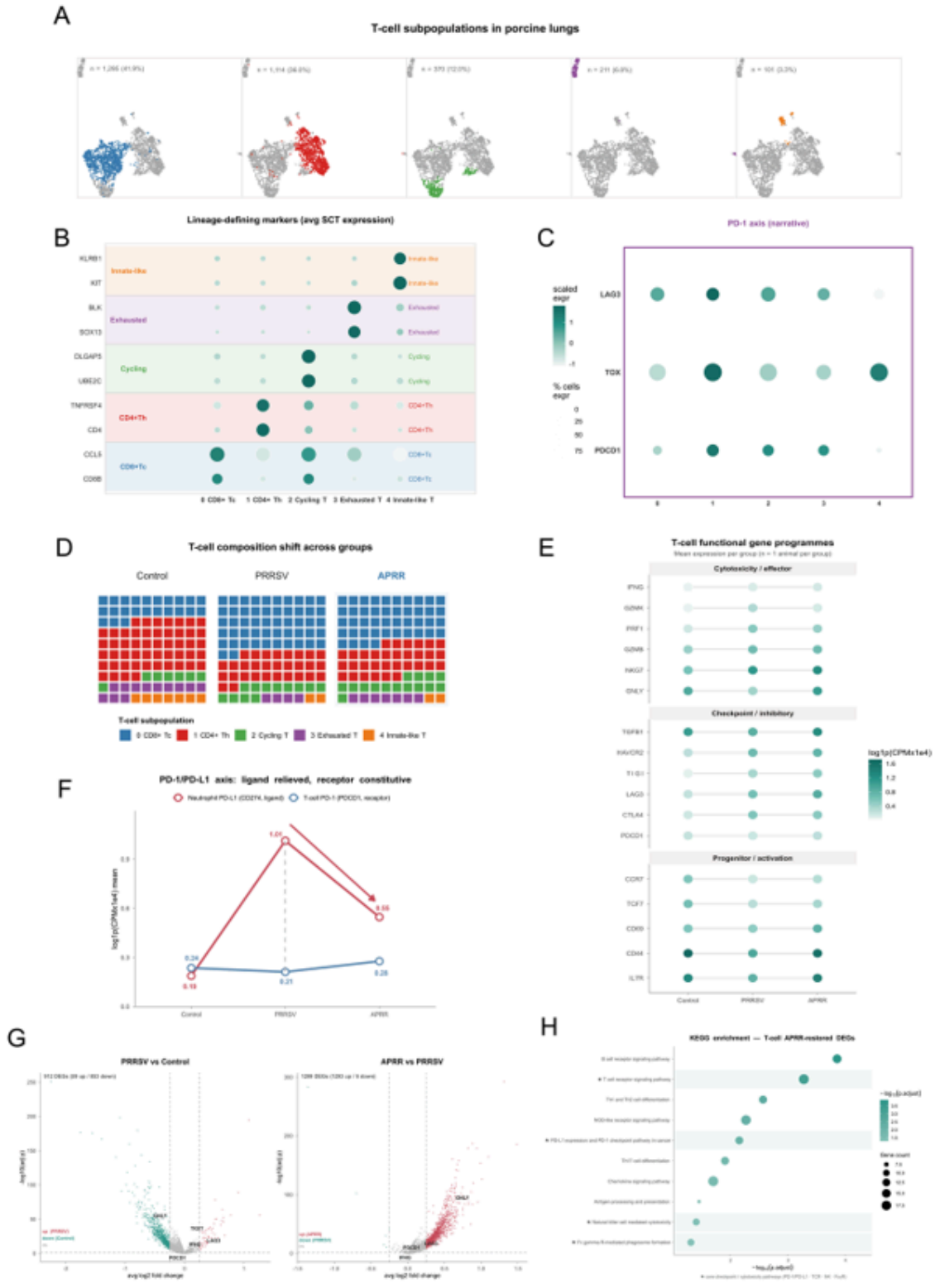


Figure 4

APRR partially restores T-cell effector programs without reversing the exhausted state. T cells resolved into five subclusters (A) annotated by lineage-defining markers (B) and a PD-1-axis schema (C). Compositional shift across groups (D). T-cell functional gene programs (E), grouped as cytotoxicity/effector, checkpoint/inhibitory and progenitor/activation; dot fill encodes mean expression. PD-1/PD-L1 axis: ligand relieved, receptor constitutive (F). Dual volcano of PRRSV- and APRR-responsive T-cell DEGs (G). KEGG enrichment of APRR-restored T-cell DEGs (H)

Fig. S4 provides the full T-cell panel: UMAPs by cell type and group (A, B), $CD4^+$:$CD8^+$ proportions (C, D), checkpoint feature and violin plots (E, F), the DEG heat map (G) and exhaustion-score, GZMB and distribution plots (H–J).

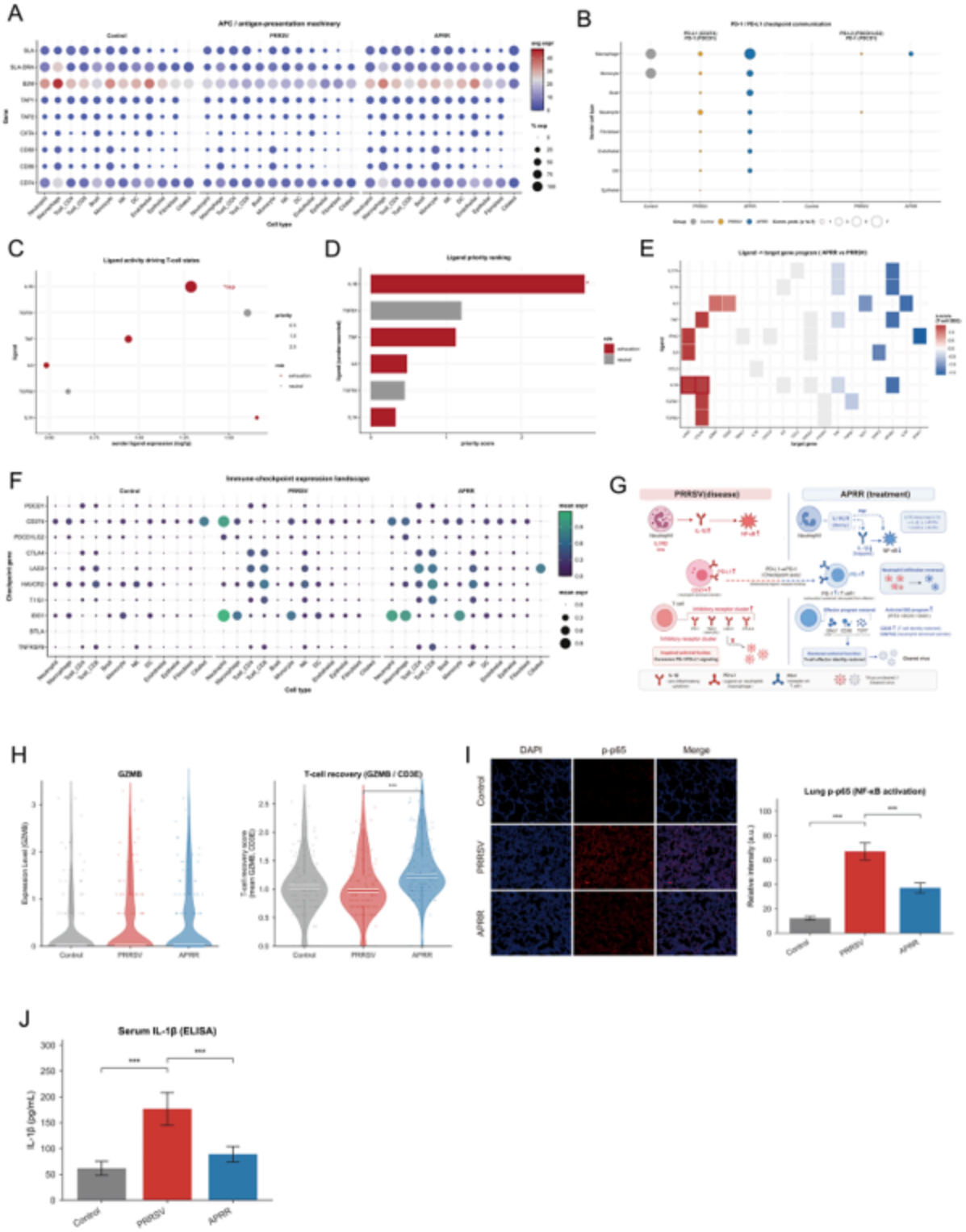


Figure 5

APRR attenuates neutrophil-centered PD-L1/PD-1 checkpoint signaling and partially restores T-cell effector programs: a dual-axis, four-pillar working model. (A) Global antigen-presentation (APC) machinery dot plot. (B) PD-1/PD-L1 and PD-1/PD-L2 checkpoint-communication plot (CellChat). (C, D) Ligand activity and priority ranking from literature-curated ligand–target scoring. (E) Ligand → target gene program heat map. (F) Inhibitory-checkpoint expression across T-cell subsets. (G) Integrated

schematic; dashed arrows with question marks denote inferred, not experimentally validated, steps, the '?' marking the IL1R2 → IL-1β step. (H) T-cell recovery at single-cell resolution: GZMB single-gene expression across groups (left; n = 777 / 1,129 / 1,185 total T cells) and a composite recovery score per cell, mean of GZMB and CD3E (right; *** APRR vs PRRSV). (I) Lung phospho-p65 immunofluorescence, an NF-κB activation readout; representative images (DAPI, p-p65, merged) and quantification (n = 4 animals per group; 44.6% reduction vs PRRSV, p = 8.2×10⁻⁴, Welch's t; values in Results). (J) Serum IL-1β ELISA (n = 6 animals per group; 49.6% reduction vs PRRSV, p = 4.5×10⁻⁴, Welch's t; values in Results). (I, J) show that IL1R2 transcript-level induction is accompanied by downstream IL-1β protein reduction and NF-κB dampening, whereas the IL1R2 → IL-1β step itself remains inferred (see G)

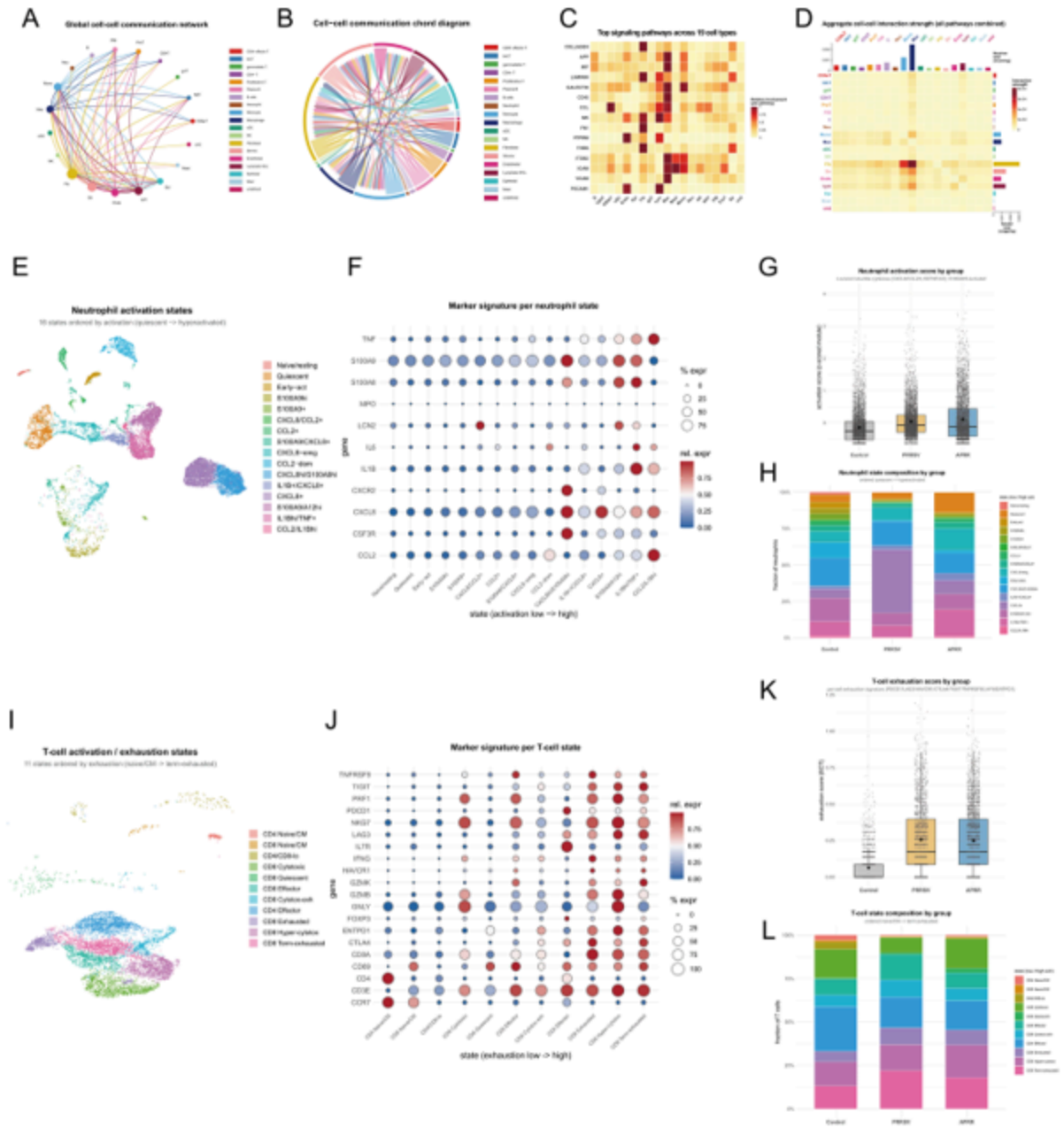


Figure 6

Integrated cell–cell communication and activation-state analyses (CellChat and literature-curated ligand–target scoring). (A–D) Global communication network across groups: pathway-enriched network (A), chord (B), and heatmaps (C, D). (E–H) Neutrophil activation states: 16-state UMAP (E), 11-marker dot plot (F), activation score (G), and 16-state composition (H). (I–L) T-cell states: 11-state UMAP (I), 20-marker dot plot (J), exhaustion score (K), and 11-state composition (L). CellChat outputs are inferred / predicted

Supplementary Files

This is a list of supplementary files associated with this preprint. Click to download.

- ESM1.pdf